Computers & Geosciences 159 (2022) 105017

Contents lists available at ScienceDirect

Computers and Geosciences

journal homepage: www.elsevier.com/locate/cageo

3D Quantum Cuts for automatic segmentation of porous media in tomography images

Junaid Malik [f,*], Serkan Kiranyaz [a], Riyadh I. Al-Raoush [a], Olivier Monga [b], Patricia Garnier [c], Sebti Foufou [d], Abdelaziz Bouras [a], Alexandros Iosifidis [e], Moncef Gabbouj [f], Philippe C. Baveye [g]

[a] Qatar University, Doha, 2713, Qatar
[b] Institute of Research for Development, Marseille, France
[c] French National Institute for Agricultural Research, INRA, France
[d] University of Burgundy, France
[e] Aarhus University, Aarhus, Denmark
[f] Tampere University, Tampere, Finland
[g] Saint Loup Research Institute, France

ARTICLE INFO

Keywords:
Computed micro-tomography
Soil segmentation
Porous media
Graph cuts

ABSTRACT

Binary segmentation of volumetric images of porous media is a crucial step towards gaining a deeper understanding of the factors governing biogeochemical processes at minute scales. Contemporary work primarily revolves around primitive techniques based on global or local adaptive thresholding that have known common drawbacks in image segmentation. Moreover, the absence of a unified benchmark prohibits quantitative evaluation, which further undermines the impact of existing methodologies. In this study, we tackle the issue on both fronts. First, by drawing parallels with natural image segmentation, we propose a novel, and automatic segmentation technique, 3D Quantum Cuts (QCuts-3D) grounded on a state-of-the-art spectral clustering technique. Secondly, we curate and present a publicly available dataset of 68 multiphase volumetric images of porous media with diverse solid geometries, along with voxel-wise ground truth annotations for each constituting phase. We provide comparative evaluations between QCuts-3D and the current state-of-the-art over this dataset across a variety of evaluation metrics. The proposed systematic approach achieves a 26% increase in AUROC (Area Under Receiver Operating Characteristics) while achieving a substantial reduction of the computational complexity over state-of-the-art competitors. Moreover, statistical analysis reveals that the proposed method exhibits significant robustness against the compositional variations of porous media.

1. Introduction

Rapid advances in micro-CT technology and easier access to scanning hardware have made X-ray computed tomography imaging quite popular among soil scientists (Al-Raoush, 2012; Baveye et al., 2018; Kemgue et al., 2019; Pot et al., 2015). This technology facilitates the visualization and quantitative analysis of the characteristics of porous media in a non-invasive manner at micrometric scales. Data are acquired from tomography generally as grayscale 3D volumetric images where the intensity at each spatial location is proportional to the X-ray attenuation properties of the material present at the corresponding location in the scanned sample. These high-resolution volumetric images enable researchers to model, predict and better understand the biogeochemical processes occurring within the porous media at fine scales (Baveye et al., 2018; Dullien, 1992; Kravchenko et al., 2011). An essential step in this quest is segmentation - identifying populations of voxels, associated with distinct phases or constituents. The most common approach in this regard is binarization (or binary segmentation), which consists of distinguishing two phases corresponding to pore space (void) and solids.

Over the years, a substantial amount of research has been conducted towards testing existing image processing methods as well as devising novel schemes to tackle the segmentation problem (Iassonov et al., 2009; Tuller et al., 2013; Wang et al., 2011). Prevalent methods essentially employ a thresholding operation and are commonly categorized as either global, when they employ a single threshold value to categorize voxels, or local, when they aim to label individual voxels based on the

* Corresponding author.
E-mail address: junaid.malik@tuni.fi (J. Malik).

https://doi.org/10.1016/j.cageo.2021.105017
Received 10 September 2020; Received in revised form 22 October 2021; Accepted 29 November 2021
Available online 2 December 2021

intensity information in their local neighborhood. Thorough visual and quantitative comparisons (Iassonov et al., 2009) have proven global methods (Otsu, 1979; Ridler and Calvard, 1978) to be less robust toward global intensity variation, which arises due to poor contrast and partial volume effect. Local methods remedy this by accounting for the local spatial image information (Oh et al., 1999). However, the best-performing methods among them generally require a skilled operator's intervention. While valiant efforts have been made to address some of the shortcomings (Schlüter et al., 2010), the efficacy of these methods still depends on key factors such as choice of pre-filtering and design parameters, which inevitably lead to subjectivity in their use (Hapca et al., 2013). Furthermore, collectively, most of the aforementioned techniques rely on a distinctive behavior of the histogram, either globally or within local windows, which makes them prone to inadequate results when dealing with complex distributions. This is echoed by the findings of numerous studies that report a lack of efficient, unsupervised segmentation regimes tailored specifically for volumetric images of porous media (Baveye et al., 2010; Iassonov et al., 2009; Tuller et al., 2013; Wang et al., 2011). Despite the popularity of thresholding-based methods for the segmentation of porous media images, it is worth noting that such techniques are rarely used for relevant tasks in natural images (Fig. 1).

Salient-object detection is a major area of interest in computer vision research that deals with identifying visually unique and prominent regions in natural images (Borji, 2015). The task is similar to the binary segmentation of porous media representations in the key sense that both are concerned with identifying a single texturally homogenous and unique region of interest (salient-object/solids) from the backdrop (background/pore-space) in a *one-vs-rest* fashion. Based on this, salient object detection methods are more suitable for application to porous media images as opposed to classical thresholding techniques. However, the field of salient object detection is ripe with numerous novel contributions and the choice of a suitable method for application to porous media images is critical. In an extensive exploratory work (Borji et al., 2015), Quantum Cuts (QCuts) (Aytekin et al., 2016), a segmentation technique based on Quantum Mechanical principles, stood out as the best performing unsupervised method. QCuts is an automatic, unsupervised, and class-independent salient object detection method that operates on graph-based data representations. Based on these key features, it lends itself to an application for the segmentation of porous media images.

Another critical factor hindering progress regarding the segmentation of porous media images is the absence of an annotated benchmark dataset that can be used to qualitatively and quantitatively evaluate segmentation methods. Curation of such datasets is not trivial for the case of naturally occurring porous media such as real soils, because obtaining a voxel-wise ground truth is not possible (Hapca et al., 2013; Wang et al., 2011). Morphological characteristics such as porosity comparisons are often used to gauge the segmentation accuracy. However, such measures may not be adequate as the total porosity of a soil sample is often affected by pores that might not be visible at the studied X-ray resolution (Al-Raoush, 2012; Wang et al., 2011). As a workaround, researchers have resorted either to generating synthetic soil images of known porosity by working backward from binary images (Wang et al., 2011), or to using artificial systems whose porosities can be manually controlled (Iassonov et al., 2009). Moreover, the porosity measure itself is not descriptive enough as it only takes into account the global percentage of pores, not their local spatial distribution. This absence of benchmark datasets renders the quantifiable comparison among the segmentation results difficult.

Collectively, the evidence presented above highlights key issues concerning both the obsolescence of segmentation techniques and the

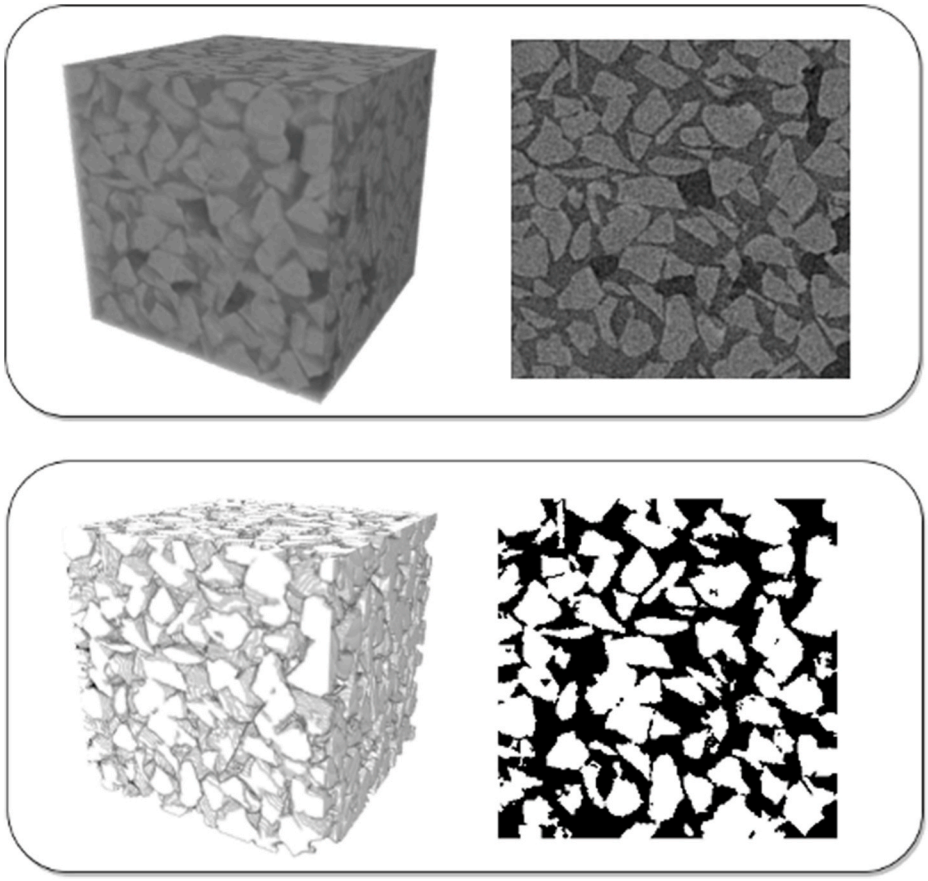

Fig. 1. 3D visualization (left) and 2D slice (right) of a test volumetric image (top) and its segmented output (bottom).

uncertainity regarding their performance owing to the absence of annotated benchmark datasets. In this study we address these two issues and make the following novel contributions:

i) QCuts-3D: an extension by 3D reformulation of the state-of-the-art 2D salient object detection method of QCuts, tailored exclusively for segmenting volumetric tomography images of porous media,
ii) SIMUPOR benchmark dataset: a collection of high-resolution multi-phase volumetric images along with expert annotated voxel-wise ground truth for each phase.

We test our method against the current state-of-the-art method of (Hapca et al., 2013) on this new dataset and calculate a variety of performance metrics that are commonly used in segmentation problems.

2. Prior work

As identified by several exploratory studies, very few of the proposed methods have been designed specifically for the segmentation of volumetric representations of porous materials. Some methods employ a 2D "slice-by-slice" approach, which has several drawbacks (Elliot and Heck, 2007; Tuller et al., 2013) and is prone to directional bias (Iassonov and Tuller, 2010). Therefore, for the sake of brevity, in this section, we restrict our discussion to methods that operate in a three-dimensional manner and have been proposed exclusively for the task of porous media segmentation. For a detailed account of other methods, the reader is referred to (Iassonov et al., 2009; Tuller et al., 2013; Wang et al., 2011).

In one of the earliest efforts (Vogel and Kretzschmar, 1996), proposed a global histogram-based approach. Initially, two threshold values; T_{min} and T_{max}, are calculated from the histogram and used to obtain a tri-partitioning of the voxels. The identified pore voxels then act as an initial seed for growing the pore space region. As an improvement (Schlüter et al., 2010), proposed to pre-process with pseudomedian filter and then calculating binary edge maps using Sobel- (SobelFeldman, 1973) and Laplace-based edge-detection. The two initial thresholds are then calculated from the histograms of each of the two edge masks. Later, Sheppard et al. (2004) proposed a multi-stage pipeline. The pre-processing step involves anisotropic filtering for denoising and unsharp masking for edge enhancement. Subsequently, a combination of watershed transform (Vincent and Soille, 1991) and a modified active contours-based seeded region growing (Kass et al., 1988) is employed. The fast marching algorithm (Forcadel et al., 2008) is used for tracking the evolution of the segmentation boundary.

Houston et al. (2013) proposed a variation on top of the widely used method of Oh et al. (1999). Instead of applying indicator kriging using a constant radius window, the authors proposed to adapt the radius based on local image conditions. After a partial prepartitioning using the method of, the spatial variance is modeled by obtaining an empirical semivariogram and fitting a theoretical model to it. The unclassified voxels are then labeled by calculating class probabilities using the kriging system. The window size is adapted progressively until a satisfactory labeling for unclassified voxels is obtained. The method was tested on 5 soil images and was shown to achieve similar results to those obtained with the method of (Oh et al., 1999) with significantly less computational cost.

In Hapca et al. (2013), a localized application of (Otsu, 1979) method is proposed. The given volume is first decomposed into non-overlapping cubes of fixed sizes. For each cube, a threshold value T_{solid} is calculated based on the profiles of the intra-class variance and phase variance functions. Afterward, an interpolation operation is applied to smooth the thresholding surface, which is finally used to obtain the desired binary segmentation. To make the critical choice of window size operator independent, the authors propose an automatic approach where a number of window sizes are tried and an optimal choice is made based on the proposed selection criterion. In the evaluation performed over a variety of synthetic soil images, the proposed method is shown to achieve a more accurate estimate of the porosity values and a lower misclassification error, compared to competing methods. Moreover, it is also completely automatic and does not require any operator intervention.

From the above overview, an obvious need for more robust and efficient unsupervised segmentation regimes arises. The performance of indicator-kriging-based methods (Houston et al., 2013; Oh et al., 1999) relies entirely on the pre-selected pair of thresholds. Despite efforts made to automate this step, as noted by (Houston et al., 2013), expert intervention is still required to get reasonable and stable outcomes. For methods involving preprocessing (Schlüter et al., 2010; Sheppard et al., 2004; Vogel and Kretzschmar, 1996), there is a significant degree of operator subjectivity related to the choice of filtering operation and tuning of the parameters involved. Furthermore, region growing-based methods (Sheppard et al., 2004), are inherently sensitive to the choice of initialization. The method of (Hapca et al., 2013) is the only fully automatic solution that does not involve manual decisions regarding the tuning of the parameters. However, this is achieved by exhaustively searching the parameter space for optimum window size. T, which involves multiple passes over the image, which is undesirable. Additionally, the shape of the window is also quite critical as cubic or spherical windows used in (Houston et al., 2013) and (Hapca et al., 2013) cannot guarantee that the contours of the solid grains will be preserved. Finally, the most crucial drawback is that all the threshold-based methods assume distinctive peaks in the gray-scale distribution. For complex images where the solid intensity varies and/or the pores are filled with different media (gas, saline water, or oil), this dependence on histograms leads to unsatisfactory results.

One of the most widely studied natural image segmentation problems is salient object detection, which, like the binarization of porous media images, aims at a one-vs-rest categorization of the image elements into the foreground (region-of-interest) and the background. In a thorough quantitive evaluation of 29 salient object detection methods over 7 different datasets (Borji et al., 2015), the method of (Aytekin et al., 2015) came out as the best among unsupervised methods. The method employs QCuts (Aytekin et al., 2014), a spectral clustering-based object segmentation technique that hinges on Quantum Mechanical principles. QCuts is uniquely distinct from the other methods in the sense that it is based on a specialized graph-cut operation and lends itself to an application on *any* graph-based data representation. Also, it is fully automatic and does not rely on labeled training examples for parameter selection or tuning. These two key factors make the native QCuts the most promising candidate for an extension to 3D pore segmentation. Therefore, the primary objective of this study was the development of a novel, highly accurate, and fast extension, QCuts-3D, orchestrated exclusively for the segmentation of digital porous media representations. The proposed method involves a single volume-to-volume mapping operation that is devoid of any parameter tuning, or redundant multiple-passes over the image.

3. Proposed methodology - QCuts-3D

In the proposed method, the contrast of the volumetric image is first adjusted as shown in Fig. 2. Then QCuts-3D proceeds as follows: a supervoxel-based representation of the volumetric image is obtained at multiple scales (Section 3.2). Then, for each scale, a graph is constructed where the nodes of the graph represent the supervoxels (Section 3.3). Using the graph cut technique of (Aytekin et al., 2016), binary labeling of the nodes is then obtained, identifying them as either solid or pore (Section 3.5). Results from each scale are finally combined in a voxel-wise majority voting scheme to obtain the desired segmentation. In Section 3.1, we shall briefly introduce the traditional QCuts method for salient-object segmentation.

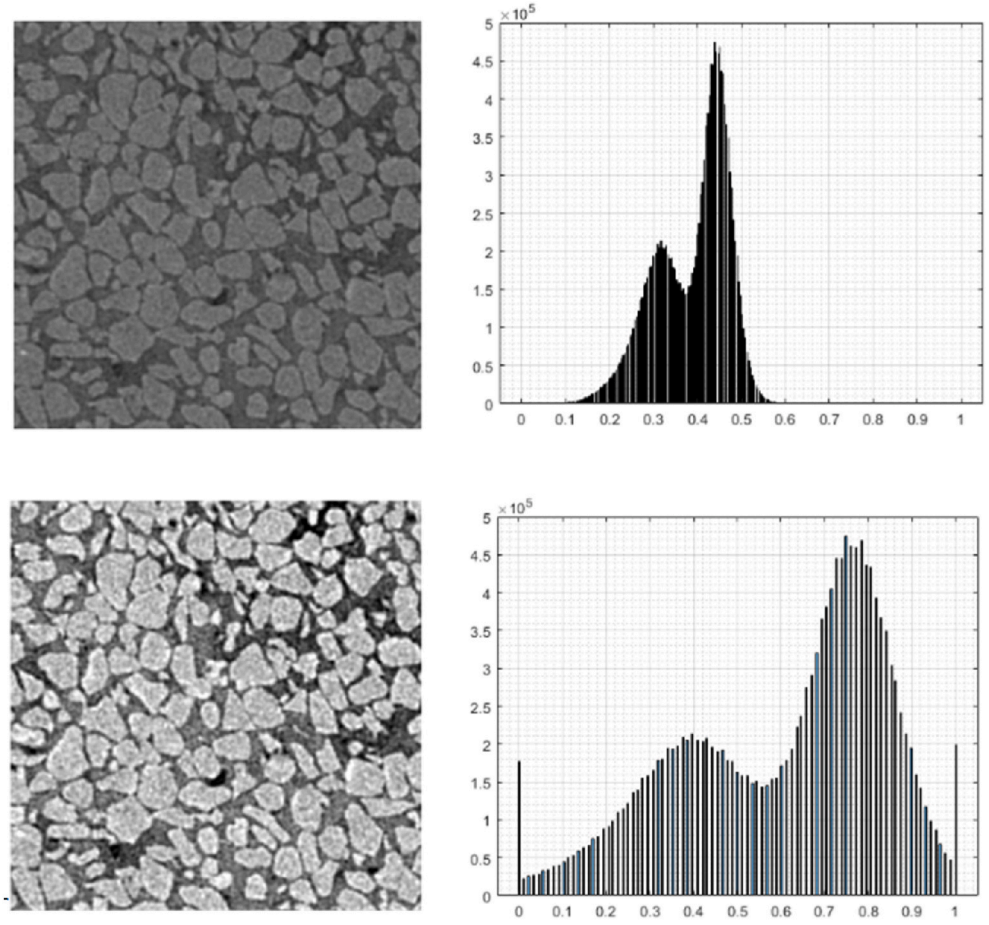

Fig. 2. 2D slice of a test original volume (top) and its contrast adjusted output (bottom) with the corresponding histograms (right).

3.1. Quantum Cuts

Image segmentation tasks are often posed as energy minimization problems where the aim is to find a labeling $\mathbf{y}$ that minimizes an energy function of the form:

$$E(\mathbf{y}) = E_{smooth}(\mathbf{y}) + E_{data}(\mathbf{y}) \tag{1}$$

In (1), the data term $E_{data}(\mathbf{y})$ encourages the labeling to be consistent with the given image information while the term $E_{smooth}(\mathbf{y})$ ensures that the labeling is smooth over neighboring image elements (Boykov et al., 2001). In the widely used framework of active contours (Kass et al., 1988), the energy is a summation of an internal energy term (smoothness term), which controls the bending of the segmentation contour, and an external energy term (data term) based on local image features such as edges, which pushes the contour towards object boundaries. Despite their popularity, active contour-based methods are quite sensitive to weights in the energy function and the choice of initialization. Moreover, they do not guarantee a globally optimum solution and can only find the local minima closest to the initialized contour (Xu et al., 2007).

Graph cut-based techniques provide a globally optimum solution to many energy minimization problems related to image segmentation (Kim and Hong, 2009; Zhou et al., 2013). The energy function to be minimized takes the following general form, (Lucchi et al., 2012):

$$E(\mathbf{y}) = E_{unary}(\mathbf{y}) + \lambda E_{binary}(\mathbf{y}) \tag{2}$$

$$E_{unary}(\mathbf{y}) = \sum_{i} \varphi(y_i) \tag{3}$$

$$E_{binary}(\mathbf{y}) = \sum_{p,q} \psi(y_p, y_q) \tag{4}$$

The unary (data) term $E_{unary}(\mathbf{y})$ measures how appropriate label y_i is for the i^{th} node given the image information. The binary (smoothness) term $E_{binary}(y)$ measures the cost of assigning disparate labels to connected neighboring nodes p and q, while λ controls the weight of these terms. It can be noted that a binary term consisting of the summation of edges to be cut is not appropriate as it favors cutting short boundaries, resulting in small isolated regions. To alleviate this, several domain-specific modifications to the energy function of (2) are generally made (Jianbo Shi et al., 1997; Wang et al., 2003).

QCuts (Aytekin et al., 2014, 2015) is specifically tailored for one-vs-rest labeling problems and produces state-of-the-art results for the task of salient-object. In QCuts, the modified energy function takes the form:

$$E_m = \frac{E_{unary}(\mathbf{y}) + E_{binary}(\mathbf{y})}{\sum_i (y_i)} \tag{5}$$

In (5), the denominator term, $\sum_i y_i$, is introduced to maximize the area of the foreground/salient region. This is a key aspect of QCuts that makes it different from other graph-cut based segmentation techniques such as (Jianbo Shi and Malik, 2000) and (Wang et al., 2003). While these methods aim at partitioning the graph into two or more homogenous regions, QCuts' optimization criterion is more inclined towards separating nodes belonging to a single region of interest (foreground) from the rest (Aytekin et al., 2016) which makes it more suitable for one-vs-rest categorization problems such as binarization of porous media images.

Given a graph-based representation of the image where the edge weight connecting node i and j is denoted as w_{ij}, the segmentation problem can be expressed, using the modified energy function, as follows:

$$\underset{\mathbf{y}}{argmin}\frac{\sum_i \varphi(y_i) + \sum_{i,j}\psi(y_i,y_j)}{\sum_i (y_i)} \tag{6}$$

where the binary potential $\psi(\mathbf{y}_i,\mathbf{y}_j)$ is defined as:

$$\psi(y_i,y_j) = w_{i,j}(y_j - y_i y_j) \tag{7}$$

And $\varphi(y_i)$ in (6) corresponds to the unary term which is explained in Section 3.4. In order to facilitate the minimization, the labeling vector $\mathbf{y}$ is replaced by another vector $\mathbf{z} = \mathbf{y} \circ \mathbf{y}$ which can take values in $[-1, 0, 1]$. Furthermore, an additional phase term is introduced to penalize sign changes of $\mathbf{z}$. Hence, the problem now becomes the following minimization:

$$\underset{\mathbf{z}}{argmin}\frac{\sum_i \varphi(z_i^2) + \sum_{i,j} w_{i,j}\left(z_j^2 - z_i^2 z_j^2\right) + \sum_{i,j} w_{i,j}\left(z_i^2 z_j^2 - z_i z_j\right)}{\sum_i (z_i^2)} \tag{8}$$

$$= \underset{\mathbf{z}}{argmin}\frac{\sum_i \varphi(z_i^2) + \sum_{i,j} w_{i,j}\left(z_j^2 - z_i z_j\right)}{\sum_i (z_i^2)} \tag{9}$$

$$= \underset{\mathbf{z}}{argmin}\frac{\mathbf{z}^T(H_m)\mathbf{z}}{\mathbf{z}^T\mathbf{z}} \tag{10}$$

In (10), the matrix H_m is expressed as follows:

$$H_m = \begin{cases} \varphi(i) + \sum_{k \in N_i} w_{ik}, if\ i = j \\ -w_{ij}, if\ i \in N_i \\ 0, otherwise \end{cases} \tag{11}$$

where N_i denotes the nodes in the neighborhood of node i. For any nonzero $\varphi(i)$, H_m is a positive definite matrix. Therefore, if the solution set of the above problem is relaxed such that $\mathbf{z} \in \mathbb{R}$, the minimization can be treated as a Rayleigh quotient problem. The solution $\mathbf{z}^*$ can then be obtained by solving the eigenvalue problem of (11). Specifically, it is the eigenvector corresponding to the smallest eigenvalue of H_m. Finally, the optimal labeling vector $\mathbf{y}^*$, which minimizes the energy function given in (6), can be calculated as shown in (12) and (13).

$$H_m\mathbf{z}^* = E_m\mathbf{z}^* \tag{12}$$

$$\mathbf{y}^* = \mathbf{z}^* \circ \mathbf{z}^* \tag{13}$$

where $\circ$ refers to the element-wise multiplication operation, also known as the Hadamard product. The obtained solution using QCuts has a theoretical correspondence with a quantum mechanical particle's location in space (Aytekin et al., 2016, 2018), hence the name "Quantum Cuts". Fig. 3 provides a visual explanation of the various steps comprising the QCuts operation.

3.2. Supervoxel-based representation in QCuts-3D

Obtaining a labeling for each voxel in a given volumetric image is computationally infeasible and it is essential to optimally reduce the processing load associated with generating individual voxel-wise labels. We propose to use a supervoxel-based representation of the volumetric image to be segmented. Supervoxels (like their 2D counterparts; superpixels) (Achanta et al., 2011) are groups of image elements (voxels) clustered together based on their distances in a high-dimensional feature space that encapsulates low-level image properties such as intensity cues and spatial information.

Consider the case of two voxels i and j, residing in a 4-dimensional space where the additional dimension corresponds to their grayscale intensities I_j and I_k. A distance between them can be calculated as follows:

$$D = \sqrt{\frac{(I_j - I_k)^2}{m^2} + \frac{(x_i - x_j)^2 + (y_i - y_j)^2 + (z_i - z_j)^2}{S^2}} \tag{14}$$

where (x_i, y_i, z_i) and (x_j, y_j, z_j) are spatial coordinates of voxels i and j respectively. For a given number of supervoxels K (*resolution*), and the total number of voxels in the image N, we generate supervoxels using the Simple Linear Iterative Clustering (SLIC) algorithm as proposed in (Achanta et al., 2011). Specifically, cluster centers are initialized at regular intervals $S = \frac{\sqrt{N}}{K}$ in the grid. Voxels are then iteratively assigned to the closest center based on (14), while cluster centers are simultaneously updated. The term m^2 in (14) is the so-called *compactness factor*, which controls the degree to which supervoxels adhere to the image gradients (edges). This formulation enables supervoxels to be compact and of nearly uniform size while also preserving regional boundaries (Stutz et al., 2018). Supervoxel generation is inherently three-dimensional in nature as D takes into account all three spatial dimensions, not just a single slice. Therefore using supervoxel-based generation makes QCuts-3D starkly different from the slice-by-slice approach used by other methods to reduce the computational complexity. By using a local representative statistic, such as the average grayscale intensity of the constituting voxels, supervoxels are treated as single entities to be labeled, thus alleviating the need for separately labeling individual voxels (Kitrungrotsakul et al., 2015; Lucchi et al., 2012; Mahapatra, 2013; Takaoka et al., 2017).

In the proposed approach, we obtain supervoxel-based oversegmentations at resolutions of 2000,4000,6000 and 8000 supervoxels per volumetric image, in order to account for the varying scale at which particles can be found in the studied porous media sample. This step is followed by constructing a graph where nodes represent supervoxels.

3.3. Graph construction in QCuts-3D

In the QCuts implementation for natural images, each node is connected to up to its fifth set of neighbors in the spatial domain, which helps in encoding contrast and textural information. Such an approach, while applicable to natural images where the object of interest is geometrically compact and texturally unique, are unsuitable for volumetric images of porous media. This is because the supervoxels belonging to the region of interest (solid) do not generally exhibit unique textural characteristics and are not situated close to each other. This is illustrated in Fig. 4 by comparing the region of interest for a natural image against a slice of a porous medium image. In the case of the natural image, the area of interest comprises a large connected patch at the center of the image having unique textural characteristics, however, in the case of a slice of a 3D volume of porous media, the area of interest is scattered across the slice and is not that well-connected.

Based on this observation, QCuts-3D uses a fully connected graph where each node is connected to every other node in the graph. For each supervoxel, the average gray-scale intensity of all the constituting voxels is taken as its representative. For defining the edge weights, we use the Gaussian weighted disparity in gray-scale intensities as the similarity metric (Cheung et al., 2018; Kitrungrotsakul et al., 2015). The final edge

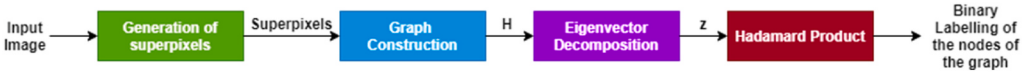

Fig. 3. Flow diagram for the Quantum Cuts-based binary segmentation.

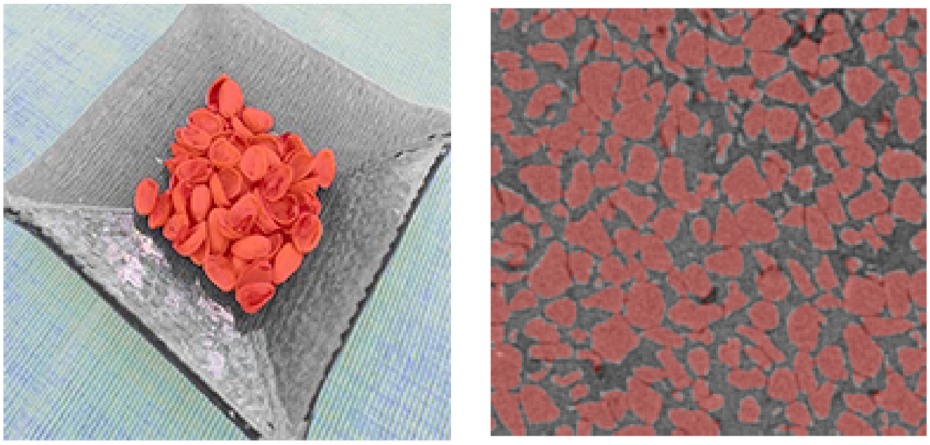

Fig. 4. Comparison of the region of interest (highlighted in red) in a natural image (left) and a 2D slice from a test volumetric image of porous media. (For interpretation of the references to color in this figure legend, the reader is referred to the Web version of this article.)

weight assignment is mathematically expressed as follows:

$$w_{ij} = \exp\left(- \frac{||S_i - S_j||_2}{2\sigma^2} \right) \tag{15}$$

where S_i is calculated as,

$$S_i = \frac{\sum \delta_{ik} I_k}{\sum \delta_{ik}} \tag{16}$$

In (16), δ_{ik} indicates whether k_{th} voxel belongs to i^{th} supervoxel

$$\delta_{ik} = \begin{cases} 1, & if\, k^{th}\ voxel \in S_i. \\ 0, & \text{otherwise.} \end{cases} \tag{17}$$

3.4. Unary potentials in QCuts-3D

In (6) and (11), the unary term $\varphi(i)$ encodes prior information about the labeling of nodes and is related to the potential of a node to belong to the background. In native QCuts, superpixels occupying the boundaries of the 2D image are assumed to belong to the background, $\varphi(i)$ is set to a very high value for these nodes and zero for all the others. However,

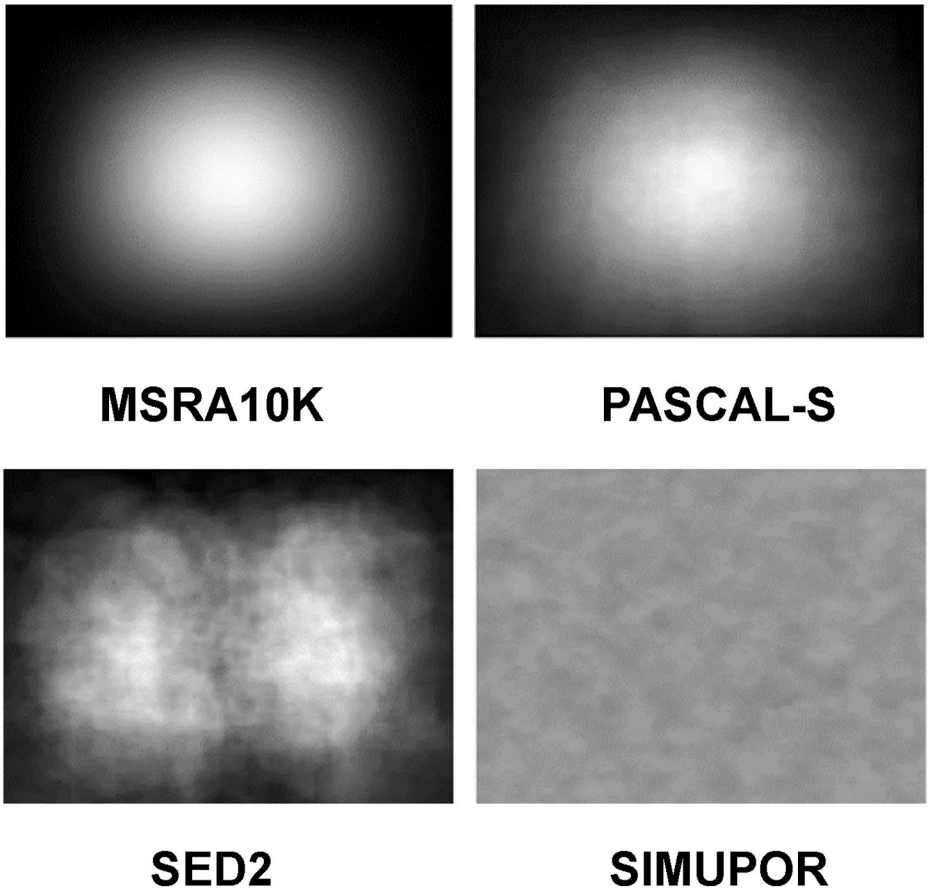

Fig. 5. Mean ground truth annotations for (Cheng et al., 2015),(Li et al., 2014),(Borji et al., 2012) (reprinted from (Borji et al., 2015)) and SIMUPOR dataset.

such a location-based prior is not suitable for the case of images of porous media. This is demonstrated in Fig. 5 which compares a pixel-wise dataset-wide average of ground truth annotations of 3 popular salient object detection datasets and 2D slices of the SIMUPOR dataset. One can clearly observe that the salient object has a noticeable location bias as it tends to reside more towards the center and rarely at the borders of the image. However, for our task, the region-of-interest (solids) is spread across the entire frame and shows no bias for any particular spatial location.

Earlier, for such volumetric images (Kulkarni et al., 2012), proposed to use a manual selection of seeds for each phase by a skilled operator. However, the authors themselves identified a need for an automated process, as manual selection makes the overall process expensive in terms of processing time and also introduces the operator's subjectivity. Moreover, owing to limitations in visualization, manual selection of seeds is not practical in the case of 3D images (Boykov et al., 2001).

In light of the aforementioned facts, in QCuts-3D, the only assumption we make about the pore space is that it occupies the lower end of the grayscale intensity distribution. Exploiting this, we slice the volumetric image along the longitudinal axis and for each slice, we perform a row-wise selection of the supervoxel with the lowest mean intensity. This set of supervoxels is denoted as $\boldsymbol{S}_{pore}$ This slice-wise approach provides a computationally economical and parameter-independent way to make sure that the initial seed selection is not affected by the global intensity variations in the given tomography data. Mathematically, the unary potential $\varphi(i)$ takes the form of a binary indicator function as follows:

$$\varphi(i) = \begin{cases} 1, & if\ S_i \in \boldsymbol{S}_{pore}. \\ 0, & \text{otherwise}. \end{cases} \tag{18}$$

3.5. Binarization in QCuts-3D

For each supervoxel resolution, we construct the graph, identify pore seeds, and then perform QCuts-3D. The initial output is a real-valued labeling vector y^* as in (13), which assigns a probability to each supervoxel corresponding to its likelihood of belonging to solid space. Finally, the output of QCuts-3D is formed by labeling the supervoxels corresponding to nodes having a high value of y^* as "solid" while the rest are labeled as "pores". Fig. 6 illustrates the proposed end-to-end pipeline.

4. Experimental results

4.1. The benchmark dataset: SIMUPOR

In this study, a benchmark dataset (aka SIMUPOR) of 68 3D volumetric images of porous media with varying grain geometry and composition is composed*. 3D volumetric images were obtained from the experiments conducted by Al-Raoush (2014) to study the effect of grain geometry on the morphology of non-aqueous phase liquids in porous media. While the contrasts between the phases in such images are good, the need to obtain an accurate and unsupervised segmentation is still present. This is extremely critical when the problem at hand involves computations of interfaces between different phases in the images such as interfacial areas and mass transfer computations. Moreover, experiments that deal with dynamic systems generate very large data that requires an unsupervised segmentation algorithm for efficient processing.

The volumes in the SIMUPOR dataset correspond to samples from 34 different experiments, each corresponding to a specific constitution of the porous medium. Among the 68 volumetric images used, 40 belong to the experiments that employ silica sand to model the porous media whereas the remaining 28 used quartz crystals. In addition to this variation in the shape of grains, there is also a variety in the size, with the median grain diameter ranging from 0.179 to 0.433 mm. This provides a comprehensive benchmark to check for the robustness of any segmentation algorithms to changes in porous media composition.

A multi-phase ground truth segmentation for the volumetric images was obtained by applying a manual skilled operator-guided process based on the indicator kriging approach (Oh et al., 1999). For each phase, images obtained from the samples scanned at different energy levels were aligned and subtracted in order to emphasize that particular phase. Afterward, segmentation for that phase was obtained by using the method of (Oh et al., 1999). Furthermore, the segmentation was verified using a variety of metrics measured independently from physical experiments of such systems. A visual example showing a slice of a test image along with its annotated ground truth is presented in Fig. 7. For more details about the image acquisition and annotation process, the reader is referred to (Al-Raoush, 2014).

4.2. Evaluation metrics

To perform the quantitative evaluation, we calculate a variety of

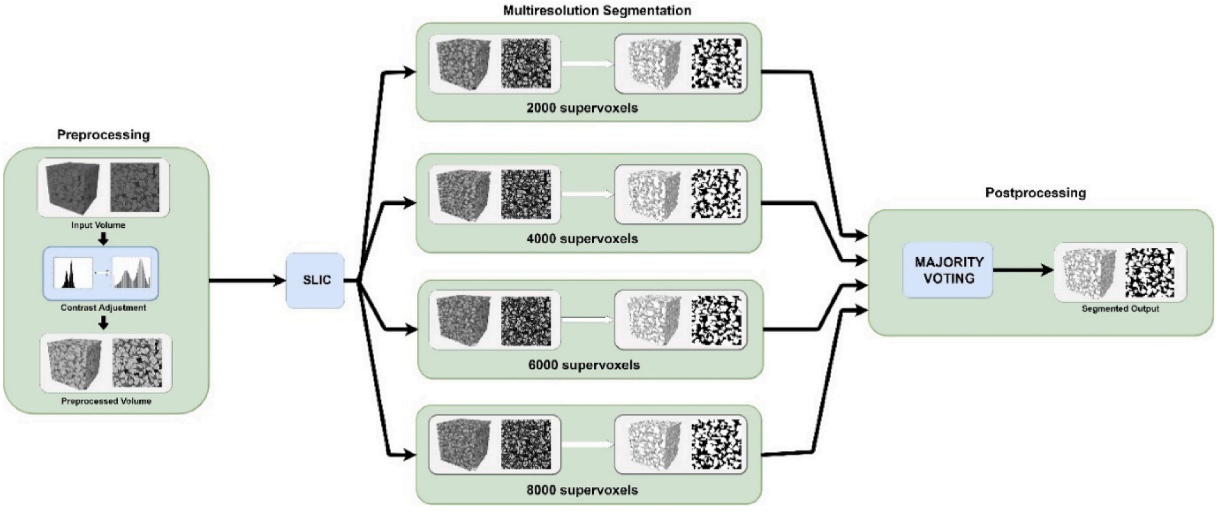

Fig. 6. The illustration of the QCuts-3D for segmentation of volumetric images of porous media. After the initial pre-processing step, a multi-resolution supervoxel-based representation of the preprocessed volume is obtained as explained in Section Supervoxel-based representation in QCuts-3D. For each supervoxel resolution, segmentation is obtained using the proposed QCuts-3D operation. Finally, outputs from all resolutions are amalgamated in a majority voting scheme to obtain the final segmented output.

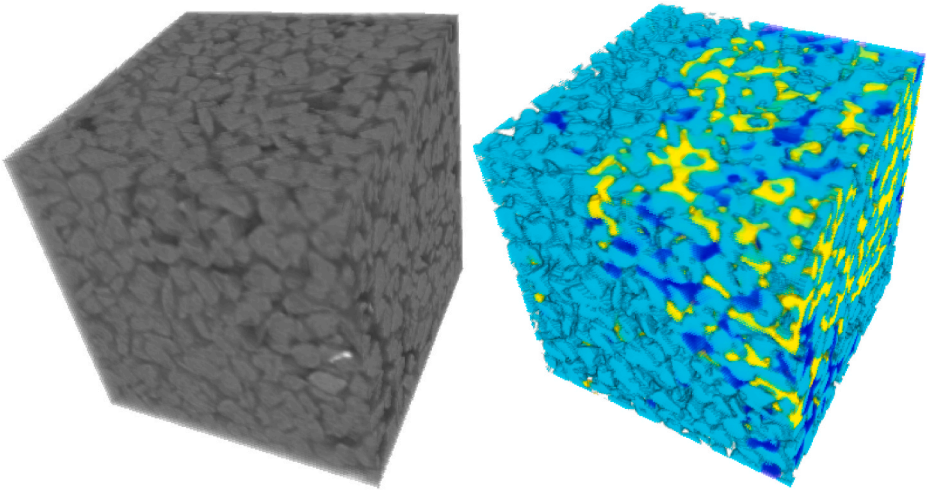

Fig. 7. 3D rendering of a sample volumetric image from SIMUPOR dataset and its manually annotated multi-phase ground truth. Solids are color-labeled as cyan while the other porous phases (water, oil, and gas) are labeled in blue, yellow, and transparent color respectively. (For interpretation of the references to color in this figure legend, the reader is referred to the Web version of this article.)

evaluation metrics to precisely measure the performance of each method. We intentionally omit evaluation criteria such as porosity, which only account for the global percentage, and fail to penalize based on localization of pore voxels within the lattice. We aim at utilizing more descriptive evaluation metrics which can efficiently penalize individual falsely labeled voxels. A brief description of each metric used and their mathematical formulations are presented as follows:

4.2.1. Jaccard Index

As originally proposed in (Jaccard, 1901), the Jaccard Index is often used to evaluate segmentation results (Everingham et al., 2010; Feng Ge et al., 2006). Also referred to as "Intersection over Union" (IoU), it is mathematically formulated as follows:

$$J(\hat{y}, y) = \frac{|\hat{y} \cap y|}{|\hat{y} \cup y|} \tag{19}$$

In (19), $\hat{y}$ is the output of segmentation, y refers to the ground truth mask, and $|.|$ is the cardinality operator.

4.2.2. Receiver operating characteristics (ROC)

ROC curves provide a two-dimensional plot with the true-positive rate (TPR) plotted on the Y-axis and the false positive rate (FPR) plotted on the x-axis. An interesting property of the ROC curve is the area under it (AUROC), which corresponds to the probability of assigning a higher score to a randomly chosen positive instance as compared to a randomly chosen negative instance (Feng Ge et al., 2006). Being a scalar, the AUROC provides a convenient way to compare classifier performance.

4.2.3. Misclassification error (ME)

Misclassification error is a simple measure and is given as the fraction of voxels that are classified incorrectly. The mathematical expression is as follows:

$$ME = \frac{False\ Positives + False\ Negatives}{Total\ number\ of\ voxels} \tag{20}$$

4.3. Performance evaluations

Table 1 and Table 2 chronicle the results of our experiments over the SIMUPOR dataset by using the aforementioned evaluation metrics. Table 2 presents the performance of the state-of-the-art automatic segmentation method of (Hapca et al., 2013) and QCuts-3D on images categorized with respect to different grain shapes. On average, QCuts-3D achieves a boost of 26% in AUROC, 23.5% in IoU, and 68.9% in ME. Similarly, Table 2 shows the same performance criteria evaluated across a variety of grain sizes. The proposed method achieves a boost of 27% in AUROC, 23% in IoU, and a 70% decrease in ME, on average. In order to evaluate the robustness of the proposed method to variations in grain geometry, we calculate the standard deviations of performances for each method across varying grain sizes and grain shapes. From our experiments, we observe that the proposed approach achieves a decrease of 28.2%, 16.1%, and 28.9% in the standard deviation of AUROC, IoU, and ME, respectively across 6 different grain sizes. Similarly, when the grain shapes are varied instead of the sizes, a performance deviation decrease of 80.8%, 45.5%, and 75.2% was observed for the three evaluation

Table 2
Performance of QCuts-3D and the competing method (Hapca et al., 2013) across different grain shapes.

	Sands		Quartz		Average	
	Hapca et al. (2013)	QCuts-3D	Hapca et al. (2013)	QCuts-3D	Hapca et al. (2013)	QCuts-3D
AUROC	0.718	**0.921**	0.740	**0.925**	0.729	**0.923**
IoU	0.725	**0.892**	0.713	**0.885**	0.719	**0.888**
ME	0.227	**0.070**	0.227	**0.0710**	0.227	**0.070**

Table 1
Performance of QCuts-3D and the competing method [13] across different grain sizes.

	d1		d2		d3		d4		d5		d6	
	Hapca et al. (2013)	QCuts-3D	Hapca et al. (2013)	QCuts-3D	Hapca et al. (2013)	QCuts-3D	Hapca et al. (2013)	QCuts-3D	Hapca et al. (2013)	QCuts-3D	Hapca et al. (2013)	QCuts-3D
AUROC	0.733	0.943	0.722	0.914	0.710	0.928	0.754	0.940	0.723	0.938	0.743	0.920
IoU	0.731	0.915	0.710	0.878	0.731	0.901	0.757	0.990	0.758	0.921	0.7000	0.872
ME	0.218	0.053	0.236	0.078	0.227	0.065	0.194	0.058	0.206	0.053	0.232	0.077

metrics, implying high robustness as compared to the competing method. This provides evidence that the QCuts-3D is more robust to variations in the grain size, compared to (Hapca et al., 2013), at least for the images included in the SIMUPOR dataset.

In terms of qualitative comparison, Fig. 8 presents the results of (Hapca et al., 2013) and QCuts-3D on the images from the SIMUPOR dataset. One can clearly observe that owing to the presence of multiple phases in the images, the adaptive thresholding technique of (Hapca et al., 2013) does not to provide adequate results. This is not surprising since the method was designed for images where it is reasonable to assume *a priori* the existence of only two very distinct populations of voxels. The method fares well in identifying the gas as the pore phase but falls short when it comes to liquid or oil phases, which have intensities closer to the solid phase.

Furthermore, the grain boundaries are also not delineated clearly as compared to the QCuts-3D. This can be attributed to the fact that local thresholding within cubical windows does not take into account regional characteristics whereas the proposed supervoxel-based representation already incorporates edge preservation and thus ensures that the regional intricacies are respected in the final segmentation outcome.

4.4. Computational complexity analysis

MATLAB implementation of QCuts-3D and (Hapca et al., 2013) were tested in MATLAB R2018a on an Intel Xeon CPU E5-2690 processor running at 2.60 GHz with 64 GB of memory. Computational efficiency

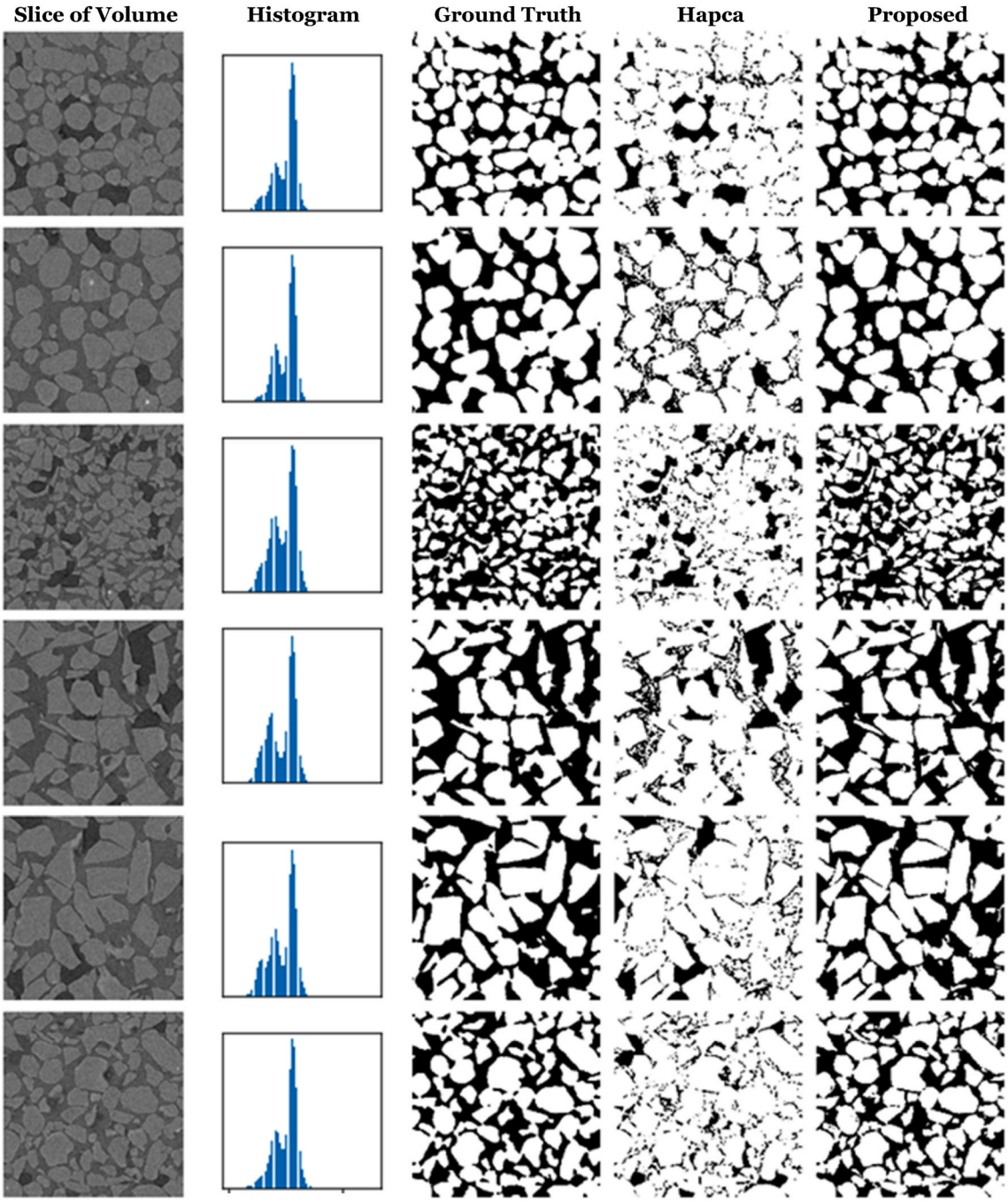

Fig. 8. Compilation of 2D slices of test images (rows) from the SIMUPOR dataset, ground truth, segmentation output of (Hapca et al., 2013) and that of QCuts-3D (from left to right). The slices correspond to columns 4,19,22,28,37 and 44 (from top to bottom), of SIMUPOR dataset.

for both methods was measured by applying them over the entire SIMUPOR dataset and averaging the run-times. On average, the competing method (Hapca et al., 2013) took 937.85 min on a single volumetric image of size 256 × 256 × 256 whereas the proposed multi-resolution scheme took only 100.96 s. This presents around 500-times less computational time due to the fact that the proposed method does not involve multiple passes over the image, and therefore is kept free from any need to repeatedly revisit the image space for parameter optimization.

5. Conclusions and future work

Local window-based segmentation methods have become the default choice for the segmentation of porous media imagery. Despite their wide usage, such methods suffer from acute reliance on manual tuning of hyperparameters. Furthermore, the shapes of local windows generally do not respect grain boundaries, resulting in segmentation artifacts. Another important hindrance towards progress in the field is the absence of annotated benchmark datasets for the evaluation of segmentation methods. In this work, we proposed a novel, automatic, and unsupervised 3D segmentation technique for porous media images. We also presented a benchmark dataset consisting of 68 multiphase volumetric images with corresponding voxel-wise segmentation ground. Furthermore, we performed an extensive comparative evaluation over this dataset, between the proposed QCuts-3D and the state-of-the-art automatic segmentation method (Hapca et al., 2013). Both quantitative and qualitative results revealed that QCuts-3D achieves a significant improvement in segmentation accuracy and computational efficiency. Moreover, it is more robust to variations in compositional elements of the pores and the geometry of the grains. Visual comparisons show that the regional boundaries are better preserved using the proposed supervoxel-based approach, as compared to localized thresholding in cubical windows employed by the competing method.

Future work involves investigating ways of improving the computational efficiency of the proposed method and extending it towards application in multiphase segmentation. We can harness the power of GPUs to expedite and parallelize the supervoxel generation step. Moreover, the introduction of the first benchmark (SIMUPOR) dataset can potentially usher in an era of a rapid influx of modern segmentation techniques such as Deep Learning-based supervised approaches, that can learn more efficient graphical representations (Aytekin et al., 2017) to segment the images using the provided ground truth annotations. Finally, we will also explore the possibility of devising multiphase segmentation approaches by utilizing the multiphase annotations of the SIMUPOR dataset.

6. Computer code availability

The code for the proposed method is written in MATLAB and named “qcuts3d 1.0”. It has been made publicly available with an open-source GPL 3.0 license at https://www.github.com/junaidmalik09/qcuts3d. The code is accompanied by a small subset of the SIMUPOR dataset to be used for testing and demo purposes. The full dataset can be obtained from https://data.mendeley.com/datasets/mx4hkgsnfn/1. Instructions for reproducing the results presented in this paper are provided in a README file.

Declaration of competing interest

The authors declare that they have no known competing financial interests or personal relationships that could have appeared to influence the work reported in this paper.

Acknowledgment

This publication was made possible by NPRP grant # NPRP9-390-1-088 from the Qatar national research fund (a member of Qatar Foundation). The findings achieved herein are solely the responsibility of the authors.

References

Achanta, R., Shaji, A., Smith, K., Lucchi, A., Fua, P., Süsstrunk, S., 2011. SLIC superpixels compared to state-of-the-art superpixel methods. Pattern analysis and machine intelligence. IEEE Transactions on 34, 2274–2282. https://doi.org/10.1109/tpami.2012.120.

Al-Raoush, R., 2012. Change in microstructure parameters of porous media over representative elementary volume for porosity. Part. Sci. Technol. 30, 1–16. https://doi.org/10.1080/02726351.2010.543262.

Al-Raoush, R.I., 2014. Experimental investigation of the influence of grain geometry on residual NAPL using synchrotron microtomography. J. Contam. Hydrol. 159, 1–10. https://doi.org/10.1016/J.JCONHYD.2014.01.008.

Aytekin, C., Kiranyaz, S., Gabbouj, M., 2014. Automatic object segmentation by quantum cuts. In: Proceedings - International Conference on Pattern Recognition, pp. 112–117. https://doi.org/10.1109/ICPR.2014.29.

Aytekin, C., Ozan, E.C., Kiranyaz, S., Gabbouj, M., 2015. Visual saliency by extended quantum cuts. In: Proceedings - International Conference on Image Processing, ICIP 2015-Decem, pp. 1692–1696. https://doi.org/10.1109/ICIP.2015.7351089.

Aytekin, Ç., Ozan, E.C., Kiranyaz, S., Gabbouj, M., 2016. Extended Quantum Cuts for Unsupervised Salient Object Extraction. Multimedia Tools and Applications. https://doi.org/10.1007/s11042-016-3431-1.

Aytekin, Ç., Iosifidis, A., Kiranyaz, S., Gabbouj, M., 2017. Learning graph affinities for spectral graph-based salient object detection. Pattern Recogn. 64, 159–167. https://doi.org/10.1016/J.PATCOG.2016.11.005.

Aytekin, C., Iosifidis, A., Gabbouj, M., 2018. Probabilistic saliency estimation. Pattern Recogn. 74, 359–372. https://doi.org/10.1016/J.PATCOG.2017.09.023.

Baveye, P.C., Laba, M., Otten, W., Bouckaert, L., Dello Sterpaio, P., Goswami, R.R., Grinev, D., Houston, A., Hu, Y., Liu, J., Mooney, S., Pajor, R., Sleutel, S., Tarquis, A., Wang, W., Wei, Q., Sezgin, M., 2010. Observer-dependent variability of the thresholding step in the quantitative analysis of soil images and X-ray microtomography data. Geoderma 157, 51–63. https://doi.org/10.1016/j.geoderma.2010.03.015.

Baveye, P.C., Otten, W., Kravchenko, A., Balseiro Romero, M., Beckers, E., Chalhoub, M., Darnault, C., Eickhorst, T., Garnier, P., Hapca, S., Monga, O., Mueller, C.W., Nunan, N., Pot, V., Schlüter, S., Schmidt, H., Vogel, H.-J.H.-J., Balseiro-Romero, M., Beckers, É., Chalhoub, M., Darnault, C., Eickhorst, T., Garnier, P., Hapca, S., Kiranyaz, S., Monga, O., Mueller, C.W., Nunan, N., Pot, V., Schlüter, S., Schmidt, H., Vogel, H.-J.H.-J., 2018. Emergent properties of microbial activity in heterogeneous soil microenvironments: different research approaches are slowly converging, yet major challenges remain. Front. Microbiol. 9, 1929. https://doi.org/10.3389/FMICB.2018.01929.

Borji, A., 2015. What is a salient object? A dataset and a baseline model for salient object detection. IEEE Trans. Image Process. 24, 742–756. https://doi.org/10.1109/TIP.2014.2383320.

Borji, A., Sihite, D.N., Itti, L., 2012. Salient Object Detection: A Benchmark. Springer, Berlin, Heidelberg, pp. 414–429. https://doi.org/10.1007/978-3-642-33709-3_30.

Borji, A., Cheng, M.-M.M., Jiang, H., Li, J., 2015. Salient object detection: a survey. IEEE Trans. Image Process. 24, 5706–5722. https://doi.org/10.1109/TIP.2015.2487833.

Boykov, Y., Veksler, O., Zabih, R., 2001. Fast approximate energy minimization via graph cuts. IEEE Trans. Pattern Anal. Mach. Intell. 23, 1222–1239. https://doi.org/10.1109/34.969114.

Cheng, M.-M., Mitra, N.J., Huang, X., Torr, P.H.S., Hu, S.-M., 2015. Global contrast based salient region detection. IEEE Trans. Pattern Anal. Mach. Intell. 37, 569–582. https://doi.org/10.1109/TPAMI.2014.2345401.

Cheung, G., Magli, E., Tanaka, Y., Ng, M.K., 2018. Graph spectral image processing. Proc. IEEE 106, 907–930. https://doi.org/10.1109/JPROC.2018.2799702.

Dullien, F.A.L., 1992. Porous Media: Fluid Transport and Pore Structure, second ed. Academic Press.

Elliot, T.R., Heck, R.J., 2007. A comparison of 2D vs. 3D thresholding of X-ray CT imagery. Can. J. Soil Sci. 87, 405–412. https://doi.org/10.4141/CJSS06017.

Everingham, M., Van Gool, L., Williams, C.K.I., Winn, J., Zisserman, A., 2010. The pascal visual object classes (VOC) challenge. IJCV 88, 303–338. https://doi.org/10.1007/s11263-009-0275-4.

Feng Ge, F., Song Wang, S., Tiecheng Liu, T., 2006. Image-segmentation evaluation from the perspective of salient object extraction. In: 2006 IEEE Computer Society Conference on Computer Vision and Pattern Recognition. IEEE, pp. 1146–1153. https://doi.org/10.1109/CVPR.2006.147. Volume 1 (CVPR'06).

Forcadel, N., Le Guyader, C., Gout, C., 2008. Generalized fast marching method: applications to image segmentation. Numer. Algorithm. 48, 189–211. https://doi.org/10.1007/s11075-008-9183-x.

Hapca, S.M., Houston, A.N., Otten, W., Baveye, P.C., 2013. New local thresholding method for soil images by minimizing grayscale intra-class variance. Vadose Zone J. 12 https://doi.org/10.2136/vzj2012.0172, 0.

Houston, A.N.N., Otten, W., Baveye, P.C.C., Hapca, S., 2013. Adaptive-window indicator kriging: a thresholding method for computed tomography images of porous media. Comput. Geosci. 54, 239–248. https://doi.org/10.1016/j.cageo.2012.11.016.

Iassonov, P., Tuller, M., 2010. Application of segmentation for correction of intensity bias in X-ray computed tomography images. Vadose Zone J. 9, 187. https://doi.org/10.2136/vzj2009.0042.

Iassonov, P., Gebrenegus, T., Tuller, M., 2009. Segmentation of X-ray computed tomography images of porous materials: a crucial step for characterization and quantitative analysis of pore structures. Water Resour. Res. 45 https://doi.org/10.1029/2009WR008087.

Jaccard, P., 1901. Étude comparative de la distribution florale dans une portion des Alpes et des Jura. Bulletin del la Société Vaudoise des Sciences Naturelles 37.

Kass, M., Witkin, A., Terzopoulos, D., 1988. Snakes: active contour models. Int. J. Comput. Vis. 321–331. https://doi.org/10.1007/BF00133570.

Kemgue, A.T., Monga, O., Moto, S., Pot, V., Garnier, P., Baveye, P.C., Bouras, A., 2019. From spheres to ellipsoids: speeding up considerably the morphological modeling of pore space and water retention in soils. Comput. Geosci. https://doi.org/10.1016/j.cageo.2018.11.006.

Kim, J.-S., Hong, K.-S., 2009. Color–texture segmentation using unsupervised graph cuts. Pattern Recogn. 42, 735–750. https://doi.org/10.1016/J.PATCOG.2008.09.031.

Kitrungrotsakul, T., Chen, Y.-W., Han, X.-H., Lin, L., 2015. Supervoxels based graph cut for medical organ segmentation. IFAC-PapersOnLine 48, 70–75. https://doi.org/10.1016/J.IFACOL.2015.10.117.

Kravchenko, A., Falconer, R.E., Grinev, D., Otten, W., 2011. Fungal colonization in soils with different management histories: modeling growth in three-dimensional pore volumes. Ecol. Appl. 21, 1202–1210. https://doi.org/10.1890/10-0525.1.

Kulkarni, R., Tuller, M., Fink, W., Wildenschild, D., 2012. Three-dimensional multiphase segmentation of X-ray CT data of porous materials using a bayesian markov random field framework. Vadose Zone J. 11 https://doi.org/10.2136/vzj2011.0082, 0.

Li, Y., Hou, X., Koch, C., Rehg, J.M., Yuille, A.L., 2014. The secrets of salient object segmentation. In: 2014 IEEE Conference on Computer Vision and Pattern Recognition, pp. 280–287. https://doi.org/10.1109/CVPR.2014.43.

Lucchi, A., Smith, K., Achanta, R., Knott, G., Fua, P., 2012. Supervoxel-based segmentation of mitochondria in EM image stacks with learned shape features. IEEE Trans. Med. Imag. 31, 474–486. https://doi.org/10.1109/TMI.2011.2171705.

Mahapatra, D., 2013. Graph cut based automatic prostate segmentation using learned semantic information. In: 2013 IEEE 10th International Symposium on Biomedical Imaging. IEEE, pp. 1316–1319. https://doi.org/10.1109/ISBI.2013.6556774.

Oh, W., Lindquist, W.B., Oh, Wonho, Lindquist, B., 1999. Image thresholding by indicator kriging. IEEE Trans. Pattern Anal. Mach. Intell. 21, 590–602. https://doi.org/10.1109/34.777370.

Otsu, N., 1979. A threshold selection method from gray-level histograms. IEEE Trans. Syst. Man Cybernetics 9, 62–66. https://doi.org/10.1109/TSMC.1979.4310076.

Pot, V., Peth, S., Monga, O., Vogel, L.E., Genty, A., Garnier, P., Vieublé-Gonod, L., Ogurreck, M., Beckmann, F., Baveye, P.C., 2015. Three-dimensional distribution of water and air in soil pores: comparison of two-phase two-relaxation-times lattice-Boltzmann and morphological model outputs with synchrotron X-ray computed tomography data. Adv. Water Resour. https://doi.org/10.1016/j.advwatres.2015.08.006.

Ridler, T.W., Calvard, S., 1978. Picture thresholding using an iterative selection method. IEEE Trans. Syst. Man Cybern. 8, 630–632. https://doi.org/10.1109/TSMC.1978.4310039.

Schlüter, S., Weller, U., Vogel, H.J., 2010. Segmentation of X-ray microtomography images of soil using gradient masks. Comput. Geosci. 36, 1246–1251. https://doi.org/10.1016/j.cageo.2010.02.007.

Sheppard, A.P., Sok, R.M., Averdunk, H., 2004. Techniques for image enhancement and segmentation of tomographic images of porous materials. Phys. Stat. Mech. Appl. 339, 145–151. https://doi.org/10.1016/J.PHYSA.2004.03.057.

Shi, Jianbo, Malik, J., 2000. Normalized cuts and image segmentation. IEEE Trans. Pattern Anal. Mach. Intell. 22, 888–905. https://doi.org/10.1109/34.868688.

Shi, Jianbo, Malik, J., Shi, J., Malik, J., 1997. Normalized cuts and image segmentation. IEEE Comput. Soc. Conf. Comput. Vis. Pattern Recogn. 22, 731–737. https://doi.org/10.1109/CVPR.1997.609407.

Sobel, Feldman, G, 1973. A 3x3 isotropic gradient operator for image processing. Pattern Classification Scene Anal. 271–272.

Stutz, D., Hermans, A., Leibe, B., 2018. Superpixels: an evaluation of the state-of-the-art. Comput. Vis. Image Understand. 166, 1–27. https://doi.org/10.1016/J.CVIU.2017.03.007.

Takaoka, T., Mochizuki, Y., Ishikawa, H., 2017. Multiple-organ segmentation by graph cuts with supervoxel nodes. In: 2017 Fifteenth IAPR International Conference on Machine Vision Applications (MVA), pp. 424–427. https://doi.org/10.23919/MVA.2017.7986891.

Tuller, M., Kulkarni, R., Fink, W., Anderson, S.H., Hopmans, J.W., 2013. Segmentation of X-Ray CT Data of Porous Materials: A Review of Global and Locally Adaptive Algorithms. https://doi.org/10.2136/sssaspecpub61.c8.

Vincent, L., Soille, P., 1991. Watersheds in digital spaces: an efficient algorithm based on immersion simulations. IEEE Trans. Pattern Anal. Mach. Intell. 13, 583–598. https://doi.org/10.1109/34.87344.

Vogel, H.J., Kretzschmar, A., 1996. Topological characterization of pore space in soil — sample preparation and digital image-processing. Geoderma 73, 23–38. https://doi.org/10.1016/0016-7061(96)00043-2.

Wang, S., Siskind, J.M.J.M., Wang, Song, Siskind, J.M.J.M., 2003. Image segmentation with ratio cut. IEEE Trans. Pattern Anal. Mach. Intell. 25, 675–690. https://doi.org/10.1109/TPAMI.2003.1201819.

Wang, W., Kravchenko, A.N.N., Smucker, A.J.M.J.M., Rivers, M.L.L., 2011. Comparison of image segmentation methods in simulated 2D and 3D microtomographic images of soil aggregates. Geoderma 162, 231–241. https://doi.org/10.1016/j.geoderma.2011.01.006.

Xu, N., Ahuja, N., Bansal, R., 2007. Object segmentation using graph cuts based active contours. Comput. Vis. Image Understand. 107, 210–224. https://doi.org/10.1016/J.CVIU.2006.11.004.

Zhou, H., Zheng, J., Wei, L., 2013. Texture aware image segmentation using graph cuts and active contours. Pattern Recogn. 46, 1719–1733. https://doi.org/10.1016/j.patcog.2012.12.005.